Catalysis Science & Technology

ROYAL SOCIETY OF CHEMISTRY

PAPER

View Article Online
View Journal | View Issue

Cite this: *Catal. Sci. Technol.*, 2025, **15**, 7110

Tuning the oxidative dehydrogenation of propane mechanism by Pd–B/Al_2O_3 bifunctional catalysis through suppression of gas-phase radicals and enhancement of surface-mediated pathways

Chunyan Ma,[abc] Cheng Chen,[ac] Zhenhao Hou,[ac] Zilin Yan,[ac] Fengbang Wang,[ac] Lei Bi,[ac] Maoyong Song *[abc] and Guibin Jiang[bc]

Boron-based catalysts typically promote the oxidative dehydrogenation of propane through a gas-phase radical mechanism, achieving high propylene selectivity but limited propane conversion. In this study, palladium is incorporated into B/Al_2O_3 to construct a bifunctional Pd–B/Al_2O_3 catalyst that shifts the reaction pathway from a radical-dominated route to a surface-catalyzed Langmuir–Hinshelwood mechanism. This cooperative effect increases propane conversion while maintaining the propylene selectivity. Quantitative analysis of both gaseous and surface H_2O_2 indicates a likely shift in the reaction mechanism from a gas-phase radical pathway to a surface-catalyzed process. Combined *in situ* EPR, DRIFT, and XPS analyses, along with DFT calculations, reveal that Pd sites promote propane adsorption and substantially lower the dehydrogenation barrier of C_3H_7, while adjacent $BO_x(OH)_{3-x}$ species selectively oxidize hydrogen to H_2O, mitigating over-oxidation. The presence of surface B–OH groups further improves performance, increasing propylene selectivity by approximately 5% under humidified conditions. These findings highlight a new strategy for designing efficient ODHP catalysts by harnessing bifunctional active sites to promote surface-mediated reaction pathways.

Received 14th August 2025,
Accepted 9th October 2025

DOI: 10.1039/d5cy00990a

rsc.li/catalysis

Introduction

Boron-based catalysts including boron nitride (BN),[1–9] boron carbide (B_4C),[10] boron oxide,[11,12] and supported boron materials[13–15] have attracted considerable attention for propane oxidative dehydrogenation (ODHP) due to their exceptional propylene selectivity. This performance originates from surface oxygen-functionalized boron species that initiate the reaction by abstracting hydrogen atoms from propane,[1–16] leading to two distinct mechanistic pathways. One is the well-established gas-phase radical pathway,[1–9] and the other is a surface-catalyzed pathway.[13,14]

In the radical mechanism, gas-phase C_3H_7· radicals undergo dehydrogenation to form propylene and simultaneously generate gaseous H_2O_2 as a characteristic byproduct due to radical reactions.[6,7,12,16] In contrast, the surface-catalyzed pathway involves chemisorbed intermediates in which surface-bound C_3H_7 species are dehydrogenated through interactions with lattice oxygen. In this process, hydrogen is transferred to surface OH or O sites, resulting in the formation of H_2O as the definitive byproduct.[13,14] Since direct detection of C_3H_7· radicals remains experimentally challenging, the concentration of gaseous H_2O_2 serves as a key indicator for distinguishing between the two pathways.

Although boron-based catalysts offer high propylene selectivity through radical pathway mechanisms, in which surface boron sites suppress alkoxyl radicals that lead to deep-oxidation products, they show inherently limited efficiency for propane dehydrogenation.[1–16] Surface-catalyzed ODHP mechanisms are less prevalent than radical pathways in pure boron systems due to the absence of cooperative interactions between distinct active sites. Successful ODHP requires both dehydrogenation sites for activating propane and nearby oxidation sites that convert hydrogen selectively into water. This cooperation helps drive the reaction toward propylene formation by thermodynamically removing hydrogen from the equilibrium.[17,18] Noble metals such as palladium and platinum demonstrate excellent dehydrogenation performance.[19–22] However, when used alone, they often favor unselective

[a] *Key Laboratory of Environmental Nanotechnology and Health Effects, Research Center for Eco-Environmental Sciences, Chinese Academy of Sciences, Beijing 100085, China. E-mail: smsong@rcees.ac.cn; Fax: +86 10 62918178; Tel: +86 10 62918178*
[b] *State Key Laboratory of Environmental Chemistry and Ecotoxicology, Research Center for Eco-Environmental Sciences, Chinese Academy of Sciences, Beijing 100085, China*
[c] *University of Chinese Academy of Sciences, Beijing 100049, China*

oxidation pathways. This drawback arises from the lack of specific sites for hydrogen oxidation, which leads to over-oxidation and combustion reactions instead of the desired selective dehydrogenation.

To address these limitations, we incorporated both palladium and boron onto an Al_2O_3 support to construct dual functional sites. In this configuration, palladium centers are responsible for propane dehydrogenation, while neighboring $BO_x(OH)_{3-x}$ species selectively oxidize hydrogen to H_2O. This structure satisfies the fundamental requirement for cooperative site functionality in ODHP. Catalytic performance studies revealed a significant increase in propane conversion by 22% without any loss in propylene selectivity. Colorimetric analysis of H_2O_2 and *in situ* spectroscopy further confirmed a mechanistic shift from gas-phase radical reactions to surface-mediated catalysis. This study presents a new strategy for the rational design of selective alkane dehydrogenation catalysts based on boron systems.

Experimental

Catalyst synthesis

The supported boron on aluminum oxide (B/Al_2O_3) was prepared using an impregnation method. Boric acid (H_3BO_3, AR, ≥99.5%, Macklin) was introduced to Al_2O_3 (AEROXIDE), followed by the addition of ultrapure water at a ratio of 50 ml H_2O per gram of Al_2O_3. The mixture was stirred vigorously at 50 °C until the solution was completely evaporated. The resulting product was then dried at 70 °C and calcined at 650 °C for 4 hours. These products were designated as *Y*B/Al_2O_3, with *Y* representing the weight percentage of boron.

The supported Pd–B/Al_2O_3 catalysts were prepared using a wetness impregnation method. An aqueous solution of palladium nitrate ($Pd(NO_3)_2{\cdot}2H_2O$, Macklin) was introduced to B/Al_2O_3, followed by drying at 80 °C overnight and subsequent calcination at 225 °C for 3 hours. The catalysts were designated as *X*Pd–*Y*B/Al_2O_3, where *X* and *Y* represent the weight percentages of palladium and boron, respectively. 3Au–1B/Al_2O_3 and 3Pt–1B/Al_2O_3 were synthesized using the same procedure as 3Pd–1B/Al_2O_3, with $HAuCl_4{\cdot}3H_2O$ and $H_2PtCl_6{\cdot}6H_2O$ as the respective metal precursors.

Catalyst characterization

Before undergoing XRD, STEM, XPS, NMR, EPR, Raman and DRIFTS characterization, the sample was pretreated using a four-step reduction process. The process involved the following steps: step 1: reduction at 150 °C for 30 min with a temperature ramping rate of 4 °C min^{-1}. Step 2: reduction at 200 °C for 30 min with a temperature ramping rate of 1 °C min^{-1}. Step 3: reduction at 250 °C for 30 min with a temperature ramping rate of 1 °C min^{-1}. Step 4: reduction at 490 °C for 30 min with a temperature ramping rate of 5 °C min^{-1} in a 10% H_2/N_2 balance. Prior to XRD, STEM, XPS and NMR characterization studies, the reduction catalysts were kept under O_2-free atmosphere.

X-ray diffraction (XRD) was performed using a PANalytical X'Pert3 Powder diffractometer with Cu Kα radiation (k = 0.15406 nm). The catalyst powder was placed on a silicon slice sample holder for testing. Samples for high-resolution transmission electron microscopy (HRTEM) were prepared by suspending catalyst powder in ethanol, followed by sonication and deposition on a Cu grid with a carbon film. HRTEM images were acquired using a JEM 2100F electron microscope operating at an acceleration voltage of 200 kV, equipped with Oxford energy-dispersive X-ray spectroscopy (EDS). X-ray photoelectron spectroscopy (XPS) and *in situ* XPS analysis of ODHP over catalysts were performed using an ESCALAB 250Xi (ThermoFisher) equipped with an Al Kα source. Detailed acquisition of individual elemental regions was performed at 40 eV. H_2-temperature-programmed reduction (TPR) was performed using a BSD-Chem C200 Automatic Chemisorption Analyzer. Prior to analysis, a 0.20 g sample was pretreated under He flow at 120 °C for 60 min. Subsequently, the system was cooled to 50 °C and subjected to reduction in 10% H_2/Ar with a temperature ramp of 10 °C min^{-1} to 900 °C, monitored by thermal conductivity detection (TCD). ^{11}B MAS nuclear magnetic resonance (NMR) performed on a JEOL JNM-ECZ600R spectrometer equipped with a 3.2 mm MAS probe operating at 192 MHz. The chemical shift was referenced to boric acid aqueous solution (1 mol L^{-1}), which has a chemical shift of 19.6 ppm. The ^{11}B direct polarization MAS NMR was conducted with a spinning rate of 12 kHz, 1210 scans, and a pulse delay of 3 s. ^1H MAS NMR conducted at the same spectrometer (JEOL JNM-ECZ600R) with a 3.2 mm MAS probe operating at 600 MHz. Hexafluoroisopropanol was used as the standard sample for ^1H MAS NMR quantification. The ^1H direct polarization MAS NMR was carried out with a spinning rate of 12 kHz, 88 scans, and a pulse delay of 5 s. Electron paramagnetic resonance (EPR) experiments using 5,5-dimethyl-1-pyrroline *N*-oxide (DMPO) as a spin-trapping were performed on a JEOL-FA200 spectrometer at 123 K. Samples of Pd/Al_2O_3, B/Al_2O_3 or Pd–B/Al_2O_3 (30 mg) were collected after oxidative dehydrogenation of propane at 490 °C for 10 minutes. The samples were quickly placed in a quartz cell, followed by the addition of 0.2 mL of DMPO (50 mg mL^{-1}). These samples were thawed and subjected to EPR measurements. Raman spectra were collected using a Renishaw inVia Raman microscope with an excitation wavelength of 532 nm, covering the range of 200–4000 cm^{-1} with a 20 s integration time. Catalyst powder was placed in an *in situ* cell reactor and pretreated using the aforementioned four-step reduction process. After the pretreatment, Raman spectra were recorded. Then a gas mixture of 6.2% C_3H_8/3.1% O_2 with N_2 balance was introduced, and Raman spectra were recorded after 5 hours of reaction. All *in situ* diffuse reflectance infrared Fourier transform spectroscopy (DRIFTS) spectra were acquired using a Bruker INVENIO R instrument equipped with a DRIFTS cell and a liquid nitrogen-cooled LN-MCT detector. The spectra were collected by accumulating 256 scans over the range of 600 to 4000 cm^{-1} at a resolution of 4 cm^{-1}. The catalyst underwent a four-step reduction process before DRIFTS measurements. After the pre-treatment, the temperature was maintained at 490 °C

under a 10% H_2/N_2 balance, and a baseline spectrum was recorded. After recording the baseline, the gas composition was switched to either 6.2% C_3H_8/3.1% O_2 with N_2 balance, or the same mixture with N_2 balance carrying saturated H_2O or D_2O vapor at 25 °C. Spectra were continuously recorded for 20 minutes to capture the ODHP spectrum. FT-IR spectra of adsorbed CO were obtained with the same Bruker INVENIO R instrument and liquid nitrogen-cooled LN-MCT detector. The catalyst was pre-treated using the same four-step reduction process. After pre-treatment, the catalyst was cooled down to 25 °C and exposed to nitrogen for 2 hours to remove physical adsorbed oxygen, followed by recording a baseline spectrum. Afterward, a pulse of CO was introduced, and the spectra were collected by accumulating 256 scans over the range of 600 to 4000 cm^{-1} at a resolution of 4 cm^{-1}.

Catalytic testing

The reaction was conducted in a quartz-tube reactor with an internal diameter of 10 mm. The catalyst (100 mg) was diluted with quartz sand (100 mg) and then loaded into the reactor. The catalysts were subjected to a four-step reduction process prior to the reaction. The temperature was maintained at 490 °C, and the catalyst was exposed to the reaction mixture. The total flow rate of the reaction mixture was 70 mL min^{-1}, comprising 4.4 mL of C_3H_8 and 2.2 mL of O_2 with either dry N_2 balance or N_2 balance carried saturated water vapor at 25 °C. The inverse weight hour-space velocity ($WHSV^{-1}$) was 0.29 $g_{C_3H_8}{}^{-1}$ $g_{catalyst}$ h, and the weight hour-space velocity (WHSV) was 1800 $L_{C_3H_8}$ $kg_{catalyst}{}^{-1}$ h^{-1}. To assess the effects of H_2O, the catalyst was physically mixed with a desiccant (macroporous silica gel). The desiccant activity was evaluated using quartz sand and a desiccant that was physically mixed with quartz sand. The CO and CO_2 products were analyzed using a gas chromatograph (Agilent 7890 B) equipped with a nickel furnace and an FID detector. C_3H_8, C_3H_6, C_2H_6, C_2H_4, and CH_4 were analyzed using an Agilent 6890N equipped with an FID detector. Propane conversion and propylene selectivity were determined by the equations below:

$$C_3H_6\ \text{Selectivity} = \frac{Y_{C_3H_6}}{Y_{C_3H_6} + \frac{2}{3}Y_{C_2H_6} + \frac{2}{3}Y_{C_2H_4} + \frac{1}{3}Y_{CH_4} + \frac{1}{3}Y_{CO} + \frac{1}{3}Y_{CO_2}} \times 100\%$$

$$C_3H_8\ \text{Conversion} = 1 - \frac{Y_{C_3H_8}}{Y_{C_3H_8} + Y_{C_3H_6} + \frac{2}{3}Y_{C_2H_6} + \frac{2}{3}Y_{C_2H_4} + \frac{1}{3}Y_{CH_4} + \frac{1}{3}Y_{CO} + \frac{1}{3}Y_{CO_2}} \times 100\%$$

Here, Y_i represents the mole fraction of product i in the outlet feed gas.

Quantitative characterization of H_2O_2

Preparation of H_2O_2 standards. The color reaction of potassium titanium oxalate (PTO dihydrate, 99.99%, Sigma-Aldrich, USA) with H_2O_2 was used to quantitatively characterize the concentration of H_2O_2. H_2O_2 solutions were prepared with low H_2O_2 concentrations (0, 0.02, 0.05 and 0.07 mg L^{-1}) and high concentrations (0.1, 0.5, 1, and 2 mg L^{-1}) using an H_2O_2 standard solution. Each H_2O_2 solution was mixed with a 0.1 M PTO solution in a 1 : 1 volume ratio. The mixed solutions (100 μL per well) were analyzed using a Microplate Reader at 400 nm to determine absorbance. A standard curve was created for low and high concentrations of H_2O_2 based on absorbance measurements.

H_2O_2 measurement from reaction gas. The catalyst (100 mg) was placed in a quartz-tube reactor with an internal diameter of 10 mm. The catalysts were pretreated using a four-step reduction process. A reaction mixture of 3% C_3H_8/1.5% O_2/N_2 was passed through the reactor at a total flow rate of 70 mL min^{-1} and 490 °C for 1 h. After the reaction, 1 mL of ultrapure water (18.2 MΩ cm, Rephile) was used to collect and dissolve liquid drops containing gaseous H_2O_2 from the condenser's quartz tube. The resulting solution was mixed with PTO and analyzed as described above.

H_2O_2 measurement on the catalyst surface. The catalyst (100 mg) was removed from the quartz tube reactor and dispersed in 1 mL of ultrapure water. The suspension was then centrifuged at 10 000 rpm for 10 min. The upper layer was collected for H_2O_2 quantification using the PTO method as described previously.

DFT calculation details

Density functional theory (DFT) calculations were performed using the projector-augmented plane-wave method in the Vienna *ab initio* simulation package. A generalized gradient approximation using the Perdew–Burke–Ernzerhof functional was used. The cutoff energy for the plane wave was set to 480 eV. The energy criterion was set to 10^{-4} eV in the iterative solution of the Kohn–Sham equation. All structures were relaxed until the residual forces on the atoms were less than 0.05 eV $Å^{-1}$. A distance of 20 Å was used in the vertical direction to prevent interactions between the periodic units. A Monkhorst–Pack scheme with a 2 × 3 × 1 *k*-point mesh was used. The nudge elastic band (CI-NEB) method was used to explore the diffusion barrier of adsorbed hydrogen at different adsorption sites.

Results and discussion

The catalytic performances of ODHP

The catalytic performances of the $1B/Al_2O_3$, $3Pd/Al_2O_3$, *X*Pd–1B/Al_2O_3, and 3Pd–*Y*B/Al_2O_3 catalysts (where *X* and *Y* represent the weight percentages of Pd and B, respectively) were compared after 1 h of reaction to assess their efficiency in propane conversion and propylene selectivity. As shown in Fig. 1a, the $3Pd/Al_2O_3$

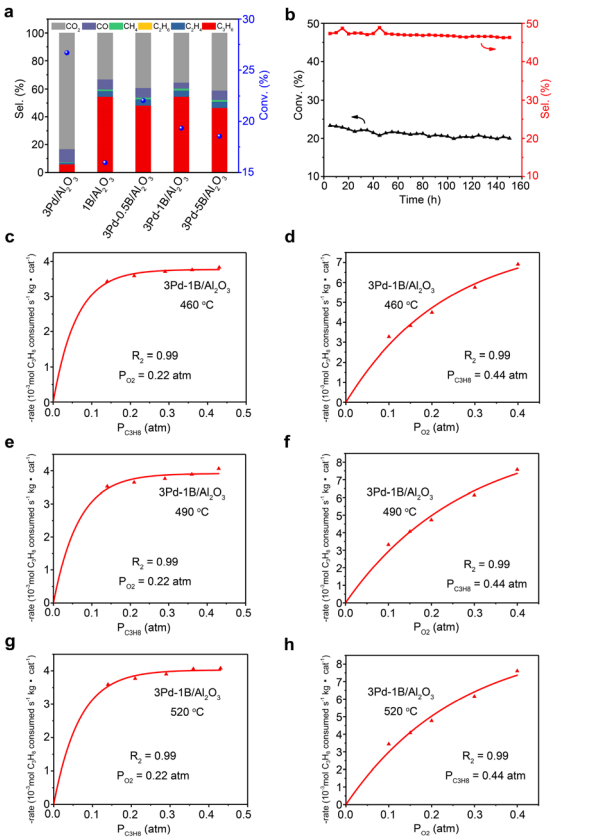

Fig. 1 (a) Catalytic performance of ODHP over 3Pd/Al_2O_3, 1B/Al_2O_3 and 3Pd–*Y*B/Al_2O_3 catalysts after 1 hour. (b) Propane conversion and propylene selectivity over time on stream for 3Pd–1B/Al_2O_3. Conditions: 490 °C, $WHSV^{-1}$ = 0.29 $g_{C_3H_8}^{-1}$ $g_{catalyst}$ hours, WHSV = 1800 $L_{C_3H_8}$ $kg_{catalyst}^{-1}$ h^{-1}, $P_{C_3H_8}:P_{O_2}:P_{N_2}$ = 4.4 : 2.2 : 93.4 kPa. (c) Rates of propane consumption using 3Pd–1B/Al_2O_3 as a function of $P_{C_3H_8}$ (P_{O_2} constant at 0.22 atm) at 460 °C. (d) Rates of propane consumption using 3Pd–1B/Al_2O_3 as a function of P_{O_2} ($P_{C_3H_8}$ constant at 0.44 atm) at 460 °C. (e and f) Corresponding propane consumption rates at 490 °C. (g and h) Corresponding propane consumption rates at 520 °C.

catalyst exhibit the highest propane conversion of 26.7%, but only 5.9% selectivity towards propylene. Most propane was completely oxidized to CO_2 over 3Pd/Al_2O_3. In contrast, 1B/Al_2O_3 achieved a propane conversion of 15.9% with a significantly higher propylene selectivity of 54.6%. Compared to 1B/Al_2O_3, Au–B/Al_2O_3 displayed inferior ODHP activity, while Pt–B/Al_2O_3 initially showed higher activity but suffered from poor stability, with approximately 54% loss in propane conversion after 300 min of reaction (Fig. S1 and S2). In contrast, the Pd–B/Al_2O_3 catalysts exhibited similar propylene selectivity, but notably increased propane conversion, suggesting that palladium doping enhanced propane conversion while maintaining high propylene selectivity. The performance of the Pd–B/Al_2O_3 catalysts was influenced by the atomic ratio of Pd to B. Among the *X*Pd–1B/Al_2O_3 catalysts, 3Pd–1B/Al_2O_3 exhibit the highest propane conversion of 19.3% and propylene selectivity of 54.6% after 1 h (Fig. S3 and S4). In the 3Pd–*Y*B/Al_2O_3 series, 3Pd–0.5B/Al_2O_3 exhibit a higher propane conversion of 22.1%, but a slightly lower propylene selectivity of 48.3% than that of 3Pd–1B/Al_2O_3 (Fig. S5 and S6). Consequently, 3Pd–1B/Al_2O_3 exhibited particularly high effectiveness for ODHP, attributed to its excellent propylene selectivity. As reported, H–BN achieved 79% selectivity to propylene at 14% propane conversion,[1] while the borosilicate MFI framework (BS-1) demonstrated approximately 10% propane conversion with ~55% propylene selectivity at 490 °C,[14] highlighting the strong catalytic performance of 3Pd–1B/Al_2O_3. A comparison of ODHP performance over various boron-based catalysts (Table S1) revealed notable differences. Due to the much lower $WHSV^{-1}$ of 0.29 $g_{C_3H_8}^{-1}$ $g_{catalyst}$ h, the 3Pd–1B/Al_2O_3 catalyst exhibited remarkable ODHP activity even at short contact times. In contrast, B_2O_3/SBA-15 showed superior ODHP performance at a higher $WHSV^{-1}$ of 9.4 $g_{C_3H_8}^{-1}$ $g_{catalyst}$ h, while SiB_6 demonstrated better activity at an elevated temperature of 545 °C. Notably, the 3Pd–1B/Al_2O_3 catalyst maintained stable ODHP performance over 150 hours, with only a slight decline in propane conversion (Fig. 1b).

Further kinetic experiments were performed to study the influence of reactant concentrations [partial pressures of O_2 and C_3H_8 (P_{O_2} and $P_{C_3H_8}$, respectively)] on the rate of propane consumption over the 3Pd–1B/Al_2O_3 catalyst. These experiments were aimed at identifying the active sites involved in the reaction. As shown in Fig. 1c–h, the rate of propane consumption at 460, 490 and 520 °C using 3Pd–1B/Al_2O_3 exhibits a first-order dependence on $P_{C_3H_8}$ and P_{O_2}, which follows the Langmuir–Hinshelwood (L–H) mechanism (eqn (1)). According to the L–H mechanism, two distinct active sites are involved in ODHP, one for the activation of oxygen and the other for the activation of propane, facilitating the reaction cycles. In comparison, BN catalysts typically follow the Eley–Rideal (E–R) mechanism in ODHP, where the oxygen activation of the boron species leads to hydrogen abstraction from the secondary carbon of propane.[1,8] However, in the BS-1 catalyst, the L–H mechanism was observed, with O_2 and C_3H_8 co-adsorbing on the dihydroxyl group of boron.[14] For the 3Pd–1B/Al_2O_3 catalyst, the mechanism shifted toward the L–H pathway owing to the addition of palladium, leading to enhanced propane activation and improved catalytic performance.

$$-r_{C_3H_8} = \frac{k\lambda_1\lambda_2 P_{C_3H_8} P_{O_2}}{(1+\lambda_1 P_{C_3H_8} + \lambda_2 P_{O_2})^2} \quad (1)$$

The characterization of structural and physicochemical properties

Structural and physicochemical properties were investigated to understand the nature of the active sites. XRD patterns confirm that the crystalline structure of γ-Al_2O_3 and θ-Al_2O_3 remains stable after impregnation with Pd and B (Fig. S7). EDS elemental composition and mapping reveal that Pd forms bright nanorods in the 3Pd–1B/Al_2O_3 catalyst (Fig. 2a–d). HRTEM images further demonstrate the presence of an interfacial heterostructure between the Pd nanorods and Al_2O_3, as indicated by the white dashed lines (Fig. 2e and f). This interfacial structure contributes to the interaction between Pd and Al_2O_3.

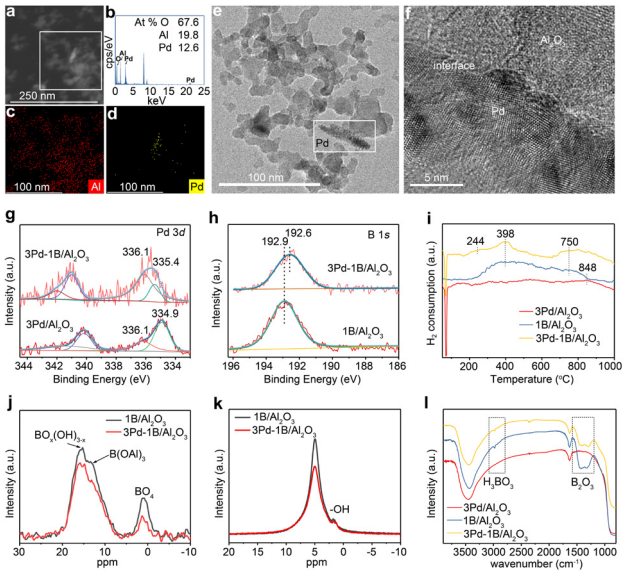

Fig. 2 (a) HRTEM image of 3Pd–1B/Al_2O_3, and (b–d) EDS elements composition and mapping of the illustrated region. (e) STEM image of 3Pd–1B/Al_2O_3, and (f) magnified view of the region marked in (e). (h) B 1s XPS spectra of 3Pd/Al_2O_3 and 3Pd–1B/Al_2O_3. (i) TPR spectra of 3Pd/Al_2O_3, 1B/Al_2O_3 and 3Pd–1B/Al_2O_3. (j) ^{11}B MAS NMR spectra of 1B/Al_2O_3 and 3Pd–1B/Al_2O_3 measured at 14.1 T. (k) ^{1}H MAS NMR spectra of 1B/Al_2O_3 and 3Pd–1B/Al_2O_3 measured at 14.1 T. (l) FTIR spectra of 3Pd/Al_2O_3, 1B/Al_2O_3 and 3Pd–1B/Al_2O_3.

Decomposition of the Pd 3d XPS spectra provides insight into the chemical state of palladium, as shown in Fig. 2g and S8. Both 3Pd/Al_2O_3 and Pd–B/Al_2O_3 catalysts exhibited two deconvoluted signals. The 3Pd/Al_2O_3 catalyst displayed Pd^0 species with a Pd $3d_{5/2}$ binding energy of 334.9 eV, along with PdO_x species at 336.1 eV.[21] For 3Pd–1B/Al_2O_3, the Pd^0 species appeared at a binding energy of 335.4 eV, while PdO_x/Pd–O–B species were also observed at 336.1 eV.[23,24] The Pd^0 binding energy in 3Pd–1B/Al_2O_3 shows a positive shift compared with that of 3Pd/Al_2O_3, indicating electron transfer from Pd to the adjacent electron-deficient B species. Additionally, the possible presence of PdO species with a Pd $3d_{5/2}$ binding energy near 337.0 eV could be excluded in either the 3Pd/Al_2O_3 or 3Pd–1B/Al_2O_3 catalysts.[25] The B 1s XPS spectrum exhibit a signal for 1B/Al_2O_3 at a binding energy of 192.9 eV, which is attributed to the B–O bond of boron oxide (Fig. 2h).[26] This signal shifts to a lower binding energy of 192.6 eV for 3Pd–0.5B/Al_2O_3 and 3Pd–1B/Al_2O_3 (Fig. 2h and S9), suggesting that the palladium atoms reduced boron *via* the Pd–O–B structure.[27]

H_2-TPR analysis was conducted to assess the redox properties of the catalysts. As shown in Fig. 2i, 3Pd/Al_2O_3 exhibited two distinct reduction peaks: a prominent negative peak at 70 °C, corresponding to hydrogen evolution from the decomposition of β-Pd–H_x, and a broad peak at 848 °C, attributed to the reduction of PdO_x species strongly interacting with the Al_2O_3 lattice.[28,29] For 1B/Al_2O_3, two reduction peaks were observed at 398 °C and 750 °C, assigned to the reduction of B_2O_3 and B–O species bonded to the Al_2O_3 lattice, respectively. Notably, 3Pd–1B/Al_2O_3 exhibited a distinct reduction peak at 244 °C, indicating a lower reduction temperature attributed to Pd-facilitated reduction of B_2O_3, likely arising from the formation of Pd–O–B species as revealed by XPS analysis.

The Raman spectrum exhibits a band at 807 cm^{-1}, indicating the presence of the B_2O_3 phase in 3Pd–1B/Al_2O_3 (Fig. S10). The molecular structure of B is investigated using 14.1 T ^{11}B NMR spectroscopy (Fig. 2j). The ^{11}B NMR signals at 15.7 and 13.2 ppm were assigned to the tricoordinated boron species, whereas the signal at 1.2 ppm was assigned to the tetracoordinated boron species.[30,31] The signal at 15.7 ppm was attributed to the boroxol-ring species associated with the terminal boron hydroxyl groups ($BO_x(OH)_{3-x}$, where x = 1 or 2), and the signal at 13.2 ppm was ascribed to the non-ring species related to the framework structure as $B(OAl)_3$.[30,31] Compared to 1B/Al_2O_3, a substantial decrease in the $B(OAl)_3$ signal in 3Pd–1B/Al_2O_3 indicated an alteration in the boron framework structure by palladium. ^{1}H NMR spectra of 1B/Al_2O_3 and 3Pd–1B/Al_2O_3 reveal split peaks at 1.2–1.8 ppm, corresponding to terminal hydroxyl groups on the Al_2O_3 surface and B sites, along with a signal at 4.9 ppm assigned to adsorbed H_2O (Fig. 2k).[14] The shift of the terminal hydroxyl group signals to a lower chemical shift in 3Pd–1B/Al_2O_3 suggests that the interaction of palladium with Al_2O_3 affects the electronegativity of these hydroxyl groups. The infrared transmission spectra of 3Pd/Al_2O_3, 1B/Al_2O_3 and 3Pd–1B/Al_2O_3 were analyzed (Fig. 2l). Compared to 3Pd/Al_2O_3, characteristic peaks corresponding to B_2O_3 were observed in the range of 1200–1600 cm^{-1} for 1B/Al_2O_3 and 3Pd–1B/Al_2O_3. In addition, peaks in the range of 2800–3000 cm^{-1} for 1B/Al_2O_3 and 3Pd–1B/Al_2O_3 were attributed to H_3BO_3, indicating the presence of BOH groups.[32]

Based on the L–H mechanism revealed by kinetic studies, two types of active sites are involved in the ODHP reaction over the 3Pd–1B/Al_2O_3 catalyst. Because the tricoordinated B species are more active than the tetracoordinated ones,[3,5,6,12] $BO_x(OH)_{3-x}$ and $B(OAl)_3$ are likely responsible for oxygen activation. Furthermore, in comparison to 1B/Al_2O_3, $BO_x(OH)_{3-x}$ species (but not the $B(OAl)_3$ species) are retained in 3Pd–1B/Al_2O_3, while the propylene selectivity remains similar between the two catalysts (Fig. 1a). This suggests that $BO_x(OH)_{3-x}$ species are the key active sites for oxygen activation. In addition, the increased propane conversion observed upon Pd doping indicates that Pd sites are likely the primary active sites for propane dehydrogenation.

The investigation of reaction pathways

To reveal the synergistic effect of the two active sites in enhancing ODHP performance, the reaction pathways over the 1B/Al_2O_3, 3Pd/Al_2O_3, and 3Pd–1B/Al_2O_3 catalysts were investigated. The production of H_2O_2 was measured both in the gas phase and on the catalyst's surface during ODHP. As shown in Fig. 3a, a gas mixture containing 6.2% C_3H_8, 3.1% O_2, and N_2 balance was passed through a heated quartz tube reactor (490 °C) containing 100 mg of the catalyst at a flow rate of 70

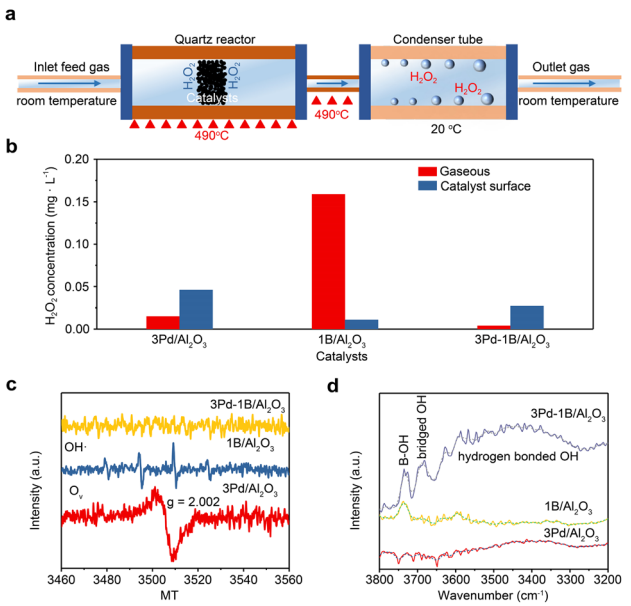

Fig. 3 (a) Schematic image of the experimental setup for measuring gaseous and catalyst surface H_2O_2 concentrations in a quartz tube reactor after ODHP reaction for 1 hour. (b) Gaseous and catalyst surface H_2O_2 concentration after 1 hour of ODHP reaction over 3Pd/Al_2O_3, 1B/Al_2O_3 and 3Pd–1B/Al_2O_3 catalysts. (c) EPR spectra of radicals after 10 minutes of ODHP reaction over 3Pd/Al_2O_3, 1B/Al_2O_3 and 3Pd–1B/Al_2O_3 catalysts. (d) DRIFT spectra after 20 minutes of ODHP reaction over 3Pd/Al_2O_3, 1B/Al_2O_3 and 3Pd–1B/Al_2O_3 catalysts.

mL min^{-1}. The effluent gas was then passed through a cooled quartz-tube (approximately 20 °C) to condense gaseous H_2O_2, which was collected over 1 h of ODHP and diluted in 1 mL of ultrapure water. Following the reaction, H_2O_2 on the catalyst surface was washed with 1 mL of ultrapure water. H_2O_2 is immediately quantified using the potassium titanium oxalate (PTO) color reaction, and the concentration is calculated using standard calibration curves (Fig. S11 and S12). As shown in Fig. 3b, the concentrations of gaseous and catalytic surface H_2O_2 are 0.159 *vs.* 0.011, 0.015 *vs.* 0.046, and 0.004 *vs.* 0.027 mg L^{-1} for 1B/Al_2O_3, 3Pd/Al_2O_3, and 3Pd–1B/Al_2O_3, respectively. These results demonstrate that boron sites primarily contribute to the formation of gaseous H_2O_2, which is typically generated *via* a radical route over boron-based catalysts.[6,7,12,16] In contrast, Pd sites predominantly generate catalyst surface H_2O_2 owing of their efficient direct H_2O_2 synthesis capabilities.[33,34] Furthermore, doping palladium onto B/Al_2O_3 significantly decreased gaseous H_2O_2 formation, likely suppressing the radical pathway.

Next, the radical species present on the catalyst surface after 10 min of ODHP were investigated using EPR. As shown in Fig. 3c, hydroxyl radicals (·OH) are observed on the 1B/Al_2O_3 catalyst, which likely originates from decomposition of gaseous H_2O_2. In contrast, oxygen vacancies (O_v) were detected in the 3Pd/Al_2O_3 catalyst, which could be attributed to the consumption of lattice oxygen during the complete oxidation of propane, following the Mars–van Krevelen mechanism.[35] Notably, neither ·OH nor O_v were detected on the 3Pd–1B/Al_2O_3 catalyst, suggesting that 3Pd–1B/Al_2O_3 inhibited the complete oxidation of propane and the formation of gaseous H_2O_2, which typically formed through the radical pathway. Subsequently, the ODHP reaction was investigated using DRIFTS. As shown in Fig. 3d, a band at 3735 cm^{-1} is observed for the 1B/Al_2O_3 and 3Pd–1B/Al_2O_3 catalysts, assignable to B–OH species. However, an additional band at 3695 cm^{-1} appeared in the spectrum of 3Pd–1B/Al_2O_3, corresponding to the bridged OH species,[36] likely BOH···C_3H_7 (or C_3H_6). This bridged OH structure indicated that the dehydrogenated C_3H_8 species (C_3H_7 or C_3H_6) were confined to the catalyst surface and interacted with the surface hydroxyl groups. These results confirmed that the 3Pd–1B/Al_2O_3 catalyst followed a surface-catalyzed reaction pathway. In addition, a broad band in the range of 3280–3550 cm^{-1}, attributed to hydrogen-bonded OH species, was observed for the 3Pd–1B/Al_2O_3 catalysts. This band is indicative of H_2O generation.[37] H_2O has previously been shown to occur in the surface-catalyzed pathway in ODHP.[13,14]

We employed quasi *in situ* XPS to investigate whether C_3H_8 and O_2 influence the chemical states of Pd and B sites on 1B/Al_2O_3, 3Pd/Al_2O_3, and 3Pd–1B/Al_2O_3 catalysts during ODHP. After 1 hour of reaction, notable changes were observed in the Pd 3d and B 1s spectra compared to the fresh catalysts (Fig. 4a to d). For 3Pd/Al_2O_3 (Fig. 4a), the Pd 3d peaks at 335.1 eV and 336.5 eV, corresponding to Pd^0 and PdO_x respectively, showed a compositional shift, with the proportion of Pd^0 increasing from 55.9% to 77.7% and PdO_x decreasing from 44.1% to 22.3%. This indicates that PdO_x was reduced during ODHP. In the case of 3Pd–1B/Al_2O_3 (Fig. 4b), the signal attributed to PdO_x/Pd–O–B species at 336.9 eV decreased from 26.9% before the reaction to nearly undetectable levels after ODHP, suggesting a transformation in the interfacial Pd–O–B

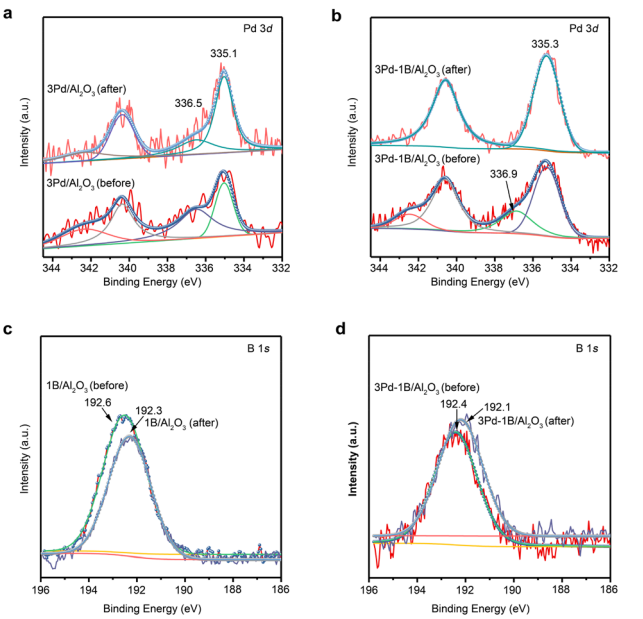

Fig. 4 Quasi *in situ* XPS spectra of the Pd 3d region for 3Pd/Al_2O_3 (a) and 3Pd–1B/Al_2O_3 (b), and the B 1s region for 1B/Al_2O_3 (c) and 3Pd–1B/Al_2O_3 (d), recorded before and after ODHP reaction for 1 h.

bonding. These results for both $3Pd/Al_2O_3$ and $3Pd–1B/Al_2O_3$ indicate that oxidized Pd species were reduced to metallic Pd^0 by hydrocarbons or hydrogen during ODHP, which can be attributed to the inherent dehydrogenation ability of Pd. In the B 1s spectra (Fig. 4c and d), both $1B/Al_2O_3$ and $3Pd–1B/Al_2O_3$ exhibited a downward shift of approximately 0.3 eV after ODHP, indicating the reduction of B–O bonds, likely due to the formation of BOH groups during the reaction, as observed in DRIFT of ODHP (Fig. 3d).

DFT calculations are conducted to further elucidate the reaction pathway of ODHP on B/Al_2O_3 (Fig. S13) and $Pd–B/Al_2O_3$ catalysts (Fig. 5). Based on structural characterization, the γ-Al_2O_3(110) surface featuring $BO_2(OH)$ sites was selected as the representative model. The γ-Al_2O_3(110) surface was chosen because it represents the most thermodynamically stable and dominant crystal facet, as confirmed by both experimental XRD reflections (Fig. S7) and previous theoretical studies. Other facets of γ-Al_2O_3 and θ-Al_2O_3, as well as $BO(OH)_2$ sites, were not studied. The adsorption energy of C_3H_8 on the BOH site differed significantly between the two catalysts: −0.196 eV for B/Al_2O_3 and −4.610 eV for $Pd–B/Al_2O_3$, indicating that C_3H_8 adsorbs much more readily on the $Pd–B/Al_2O_3$ surface. Because of the weak adsorption of propyl species on the BOH sites in B/Al_2O_3, C_3H_7 and C_3H_6 were more likely to exist as radicals than in the adsorbed states. The energy barrier for the formation of OOH from O_2 gas was 0.817 eV, whereas that for the H atom abstraction from the C_3H_7 radical to form $H_2O_2^*$ was significantly higher reaching 3.564 eV. Consequently, $H_2O_2^*$ desorption from the B/Al_2O_3 surface was more favorable, facilitating gaseous H_2O_2 formation in the radical pathway. In the radical pathway, dehydrogenation of the C_3H_7 radical (3.564 eV) represents the most energy-intensive step. In contrast, for the $Pd–B/Al_2O_3$ catalyst, the energy barrier for the dehydrogenation of C_3H_7 over a Pd site to form a Pd–H state is much lower, at just 0.334 eV (Fig. 5). The subsequent migration of the H atom from Pd to the B–O site requires slightly more energy; however, this H spillover mechanism is critical for the ODHP reaction on $Pd–B/Al_2O_3$. The primary products were C_3H_6 and H_2O obtained in this surface-catalyzed pathway aligned with the experimental results. When H_2O desorbs from the catalyst surface, it creates oxygen vacancies that are rapidly replenished by O_2, restoring the $BO_2(OH)$ sites. Therefore, the boron sites activate and provide oxygen for the oxidation of the migrated hydrogen to promote hydrogen oxidation, while inhibiting the overoxidation of hydrocarbons to CO_x. Moreover, the Pd sites facilitated propane dehydrogenation. This synergistic interaction between the two active sites in the $Pd–B/Al_2O_3$ catalyst enhanced propylene selectivity and propane conversion during the ODHP process. Raman analysis of the spent catalyst reveals characteristic bands at 1350 and 1573 cm^{-1} (Fig. S14), corresponding to graphitic carbon species,[38] indicating that carbon deposition is the main deactivation mechanism of $3Pd–1B/Al_2O_3$ during long-term ODHP testing (Fig. 1b).

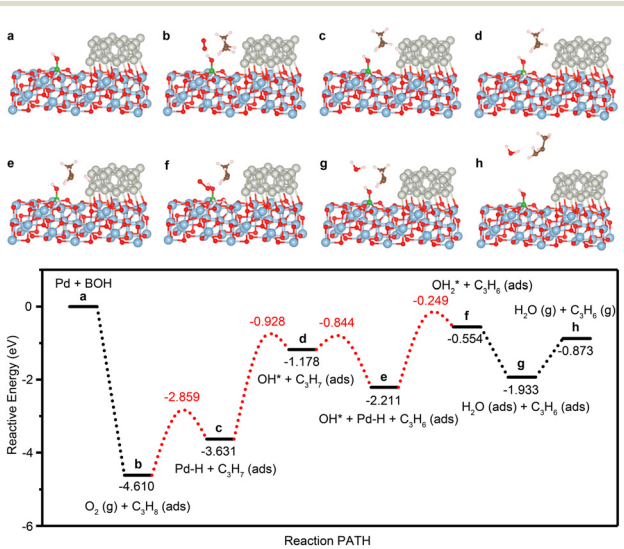

Fig. 5 DFT calculated energy profile for ODHP over $Pd–B/Al_2O_3$ following a surface-catalyzed pathway. The diagram presents the energy profile along the reaction coordinate, highlighting the initial state, transition state, and final state from left to right. The models (a–h) show side views of the geometries for the various states. The atoms are color-coded as follows: Pd in grey, B in green, Al in light blue, O in red, C in dark brown, and H in pink.

The positive effect of surface OH on ODHP

H_2O is frequently employed to enhance surface OH groups on catalysts, a strategy well supported by existing literature.[39,40] To elucidate the critical role of surface OH in ODHP, we conducted experiments using $3Pd–1B/Al_2O_3$ catalysts with systematically controlled surface OH concentrations. In these experiments, humidified feed gas was used to increase surface OH, while physically mixing the catalyst with a desiccant aimed to reduce it. Control studies confirmed that the desiccant alone had no noticeable impact on propane conversion or propylene selectivity (Fig. S15). As shown in Fig. 6a, under humid-feed conditions, propane conversion increased by approximately 0.5% and propylene selectivity by approximately 5% compared to dry-feed conditions. In contrast, introducing a desiccant to the $3Pd–1B/Al_2O_3$ catalyst significantly suppressed catalytic activity, decreasing propane conversion from 20% to 13% and propylene selectivity from 51% to 9% (Fig. 6b). These results indicate a direct correlation between surface OH concentration and ODHP performance.

DRIFT spectroscopy further supported the beneficial role of surface OH groups. During ODHP with H_2O-saturated feed, signals corresponding to B–OH and bridged OH species increased over time (Fig. 6c), whereas B–OD signals increased markedly under D_2O-saturated conditions (Fig. 6d). These findings suggest that both H_2O and D_2O dissociate to form OH (or OD) groups on the $3Pd–1B/Al_2O_3$ surface, enriching B–OH sites during ODHP. Based on these observations, we propose an ODHP reaction mechanism over $3Pd–1B/Al_2O_3$ (Fig. 6e) that begins with propane dehydrogenation at Pd sites, followed by hydrogen transfer to $BO_x(OH)_{3-x}$ sites, where oxidation occurs. The observed increase in B–OH

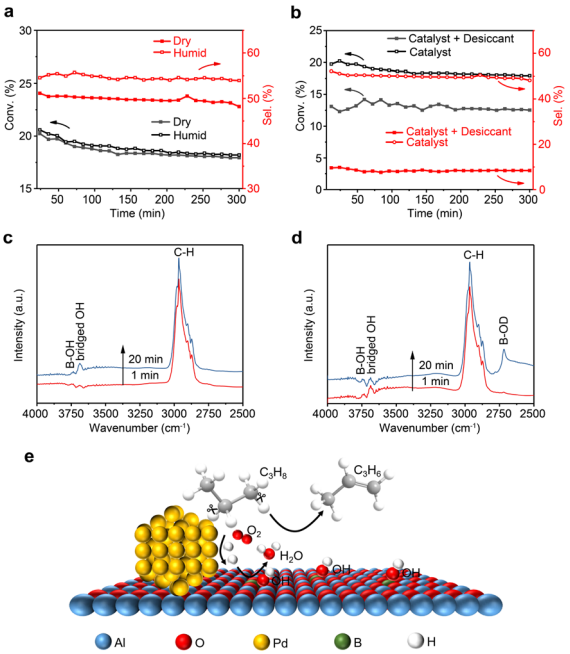

Fig. 6 (a) Propane conversion and propylene selectivity over time on stream for 3Pd–1B/Al_2O_3 in a dry feed gas and in a humid feed gas containing saturated water vapor at 25 °C. (b) Propane conversion and propylene selectivity over time on stream for 3Pd–1B/Al_2O_3 compared to 3Pd–1B/Al_2O_3 physically mixed with a desiccant. Conditions: 490 °C, $WHSV^{-1}$ = 0.29 $g_{C_3H_8}^{-1}$ $g_{catalyst}$ h, WHSV = 1800 $L_{C_3H_8}$ $kg_{catalyst}^{-1}$ h^{-1}, $P_{C_3H_8}:P_{O_2}:P_{N_2}$ = 4.4 : 2.2 : 93.4 kPa. (c) *In situ* DRIFT of ODHP with saturated H_2O gas over 3Pd–1B/Al_2O_3. (d) *In situ* DRIFT of ODHP with saturated D_2O gas over 3Pd–1B/Al_2O_3. (e) The reaction mechanism of ODHP over 3Pd–1B/Al_2O_3.

concentration is positively correlated with enhanced catalytic performance in ODHP.

Conclusions

In summary, this study demonstrates that Pd doping effectively alters the reaction mechanism of ODHP on B/Al_2O_3 catalysts. The introduction of Pd sites shifts the dominant pathway from a gas-phase radical mechanism, which is characterized by the formation of gaseous H_2O_2, to a surface-catalyzed Langmuir–Hinshelwood mechanism. Quantitative analysis of H_2O_2 shows that Pd–B/Al_2O_3 produces significantly less gaseous H_2O_2 compared to B/Al_2O_3, indicating suppression of the radical pathway. The presence of synergistic active sites enables this transition, where Pd sites promote propane adsorption and lower the activation barrier for C_3H_7 dehydrogenation, while adjacent $BO_x(OH)_{3-x}$ species selectively oxidize hydrogen to H_2O, thereby preventing over-oxidation to CO_x. The combined effect of these bifunctional sites enhances propane conversion by 22% (from 15.9% to 19.3%) while maintaining a propylene selectivity of 55%. Surface B–OH further contribute to catalytic performance, as supported by humid-feed experiments showing an approximately 5% increase in propylene selectivity. This work offers a promising strategy for designing efficient ODHP catalysts by integrating noble metals like Pd with boron-based materials to harness surface-mediated pathways and overcome limitations associated with radical mechanisms. This work offers a promising strategy for designing efficient ODHP catalysts by integrating noble metals like Pd with boron-based materials to harness surface-mediated pathways and overcome limitations associated with radical mechanisms. Future efforts to enhance the catalytic efficiency of Pd–B/Al_2O_3 will focus on tuning the Pd–B interaction through controlled dispersion and electronic modulation, as well as optimizing the support properties to achieve a better balance between propane activation and propylene selectivity.

Author contributions

C. M. performed most experiments and wrote the initial draft. C. C. contributed to discussion. Z. H. carried out catalyst synthesis. Z. Y., F. W. and L. B. contributed to a part of characterization. M. S. was responsible for supervision, review and draft revision. G. J. was responsible for review.

Conflicts of interest

There are no conflicts to declare.

Data availability

The data supporting this article have been included as part of the supplementary information (SI).

Supplementary information is available. See DOI: **https://doi.org/10.1039/d5cy00990a**.

Acknowledgements

Financial support by the National Natural Science Foundation of China (grants 22125606, 22376205, 21976198).

References

1 J. T. Grant, C. A. Carrero, F. Goeltl, J. Venegas, P. Mueller, S. P. Burt, S. E. Specht, W. P. McDermott, A. Chieregato and I. Hermans, Selective oxidative dehydrogenation of propane to propene using boron nitride catalysts, *Science*, 2016, **354**, 1570–1573.

2 H. Li, J. Zhang, P. Wu, S. Xun, W. Jiang, M. Zhang, W. Zhu and H. Li, O_2 Activation and oxidative dehydrogenation of propane on hexagonal boron nitride: Mechanism revisited, *J. Phys. Chem. C*, 2019, **123**, 2256–2266.

3 M. C. Cendejas, O. A. Paredes Mellone, U. Kurumbail, Z. Zhang, J. H. Jansen, F. Ibrahim, S. Dong, J. Vinson, A. N. Alexandrova, D. Sokaras, S. R. Bare and I. Hermans, Tracking active phase behavior on boron nitride during the oxidative dehydrogenation of propane using operando X-ray raman spectroscopy, *J. Am. Chem. Soc.*, 2023, **145**, 25686–25694.

4 Z. Zhang, J. Tian, X. Wu, I. Surin, J. Perez-Ramirez, P. Hemberger and A. Bodi, Unraveling radical and oxygenate routes in the oxidative dehydrogenation of propane over boron nitride, *J. Am. Chem. Soc.*, 2023, **145**, 7910–7917.

5 Z. Zhang, I. Hermans and A. N. Alexandrova, Off-stoichiometric restructuring and sliding dynamics of hexagonal boron nitride edges in conditions of oxidative dehydrogenation of propane, *J. Am. Chem. Soc.*, 2023, **145**, 17265–17273.

6 X. Zhang, R. You, Z. Wei, X. Jiang, J. Yang, Y. Pan, P. Wu, Q. Jia, Z. Bao, L. Bai, M. Jin, B. Sumpter, V. Fung, W. Huang and Z. Wu, Radical chemistry and reaction mechanisms of propane oxidative dehydrogenation over hexagonal boron nitride catalysts, *Angew. Chem., Int. Ed.*, 2020, **59**, 8042–8046.

7 J. M. Venegas, Z. Zhang, T. O. Agbi, W. P. McDermott, A. Alexandrova and I. Hermans, Why boron nitride is such a selective catalyst for the oxidative dehydrogenation of propane, *Angew. Chem., Int. Ed.*, 2020, **59**, 16527–16535.

8 J. Tian, J. Tan, M. Xu, Z. Zhang, S. Wan, S. Wang, J. Lin and Y. Wang, Propane oxidative dehydrogenation over highly selective hexagonal boron nitride catalysts: The role of oxidative coupling of methyl, *Sci. Adv.*, 2019, **5**, eaav8063.

9 L. Shi, D. Wang, W. Song, D. Shao, W. P. Zhang and A. H. Lu, Edge-hydroxylated Boron Nitride for Oxidative Dehydrogenation of Propane to Propylene, *ChemCatChem*, 2017, **9**, 1788–1793.

10 L. Zhu, Z. Liu, Q. Zhou, W.-D. Lu and D. Wang, Propane oxidative dehydrogenation on nanosized boron carbide: Effect of boron content and its oxidation implicated by DFT calculations, *J. Phys. Chem. C*, 2023, **127**, 6280–6293.

11 J. Tian, G. Collinge, S. F. Yuk, J. Lin, V.-A. Glezakou, M.-S. Lee, Y. Wang and R. Rousseau, Dynamically formed active sites on liquid boron oxide for selective oxidative dehydrogenation of propane, *ACS Catal.*, 2023, **13**, 8219–8236.

12 W.-D. Lu, D. Wang, Z. Zhao, W. Song, W.-C. Li and A.-H. Lu, Supported boron oxide catalysts for selective and low-temperature oxidative dehydrogenation of propane, *ACS Catal.*, 2019, **9**, 8263–8270.

13 H. Yan, S. Alayoglu, W. Wu, Y. Zhang, E. Weitz, P. C. Stair and J. M. Notestein, Identifying boron active sites for the oxidative dehydrogenation of propane, *ACS Catal.*, 2021, **11**, 9370–9376.

14 H. Zhou, X. Yi, Y. Hui, L. Wang, W. Chen, Y. Qin, M. Wang, J. Ma, X. Chu, Y. Wang, X. Hong, Z. Chen, X. Meng, H. Wang, Q. Zhu, L. Song, A. Zheng and F.-S. Xiao, Isolated boron in zeolite for oxidative dehydrogenation of propane, *Science*, 2021, **372**, 76–80.

15 R. Belgamwar, A. G. M. Rankin, A. Maity, A. K. Mishra, J. S. Gómez, J. Trébosc, C. P. Vinod, O. Lafon and V. Polshettiwar, Boron nitride and oxide supported on dendritic fibrous nanosilica for catalytic oxidative dehydrogenation of propane, *ACS Sustainable Chem. Eng.*, 2020, **8**, 16124–16135.

16 X. Gao, M. Liu, Y. Huang, W. Xu, X. Zhou and S. Yao, Dimensional understanding of boron-based catalysts for oxidative propane dehydrogenation: Structure and mechanism, *ACS Catal.*, 2023, **13**, 9667–9687.

17 H. Wang, H. Li, J. Duan, L. Wang and F. S. Xiao, Adjustment of molecular sorption equilibrium on catalyst surface for boosting catalysis, *Acc. Chem. Res.*, 2025, **58**, 440–451.

18 X. Li, G. Hai, D. H. C. Wan, Y. Liao, Z. Yao, F. Zhao, L. Huang, J. Zhou, G. Li, G. F. Chen, F. R. Wang, M. K. H. Leung and H. Wang, Favoring the originally unfavored oxygen for enhancing nitrogen-to-nitrate electroconversion, *J. Am. Chem. Soc.*, 2025, **147**, 8587–8596.

19 M. Peng, Z. Jia, Z. Gao, M. Xu, D. Cheng, M. Wang, C. Li, L. Wang, X. Cai, Z. Jiang, H. Jiang, N. Wang, D. Xiao, H. Liu and D. Ma, Antisintering Pd1 catalyst for propane direct dehydrogenation with in situ active sites regeneration ability, *ACS Catal.*, 2022, **12**, 2244–2252.

20 F. Jiang, L. Zeng, S. Li, G. Liu, S. Wang and J. Gong, Propane dehydrogenation over Pt/TiO_2–Al_2O_3 catalysts, *ACS Catal.*, 2014, **5**, 438–447.

21 P. Wang, X. Zhang, R. Shi, J. Zhao, G. I. N. Waterhouse, J. Tang and T. Zhang, Photocatalytic ethylene production by oxidative dehydrogenation of ethane with dioxygen on ZnO-supported PdZn intermetallic nanoparticles, *Nat. Commun.*, 2024, **15**, 789.

22 C. Duan, J. Liu, Z. Li, R. Shi, J. Zhao, G. I. N. Waterhouse, X. Wen, L. Zhang, L. Wu and T. Zhang, Efficient photocatalytic propane direct dehydrogenation to propylene over PtO_2 clusters, *Adv. Mater.*, 2025, **37**, 2411648.

23 S. Yue, C. S. Praveen, A. Klyushin, A. Fedorov, M. Hashimoto, Q. Li, T. Jones, P. Liu, W. Yu, M. G. Willinger and X. Huang, Redox dynamics and surface structures of an active palladium catalyst during methane oxidation, *Nat. Commun.*, 2024, **15**, 4678.

24 K. Tang, Y. Ren, W. Liu, J. Wei, J. Guo, S. Wang and Y. Yang, Insight investigation of active palladium surface sites in palladium-ceria catalysts for NO + CO reaction, *ACS Appl. Mater. Interfaces*, 2018, **10**, 13614–13624.

25 G. Wang, Y. Yan, X. Zhang, X. Gao and Z. Xie, Three-dimensional porous hexagonal boron nitride fibers as metal-free catalysts with enhanced catalytic activity for oxidative dehydrogenation of propane, *Ind. Eng. Chem. Res.*, 2021, **60**, 17949–17958.

26 Z.-L. Du, Q.-Q. Dang and X.-M. Zhang, Heptazine-based porous framework supported palladium nanoparticles for green suzuki–miyaura reaction, *Ind. Eng. Chem. Res.*, 2017, **56**, 4275–4280.

27 J. T. Grant, W. P. McDermott, J. M. Venegas, S. P. Burt, J. Micka, S. P. Phivilay, C. A. Carrero and I. Hermans, Boron and boron-containing catalysts for the oxidative dehydrogenation of propane, *ChemCatChem*, 2017, **9**, 3623–3626.

28 T. Fovanna, M. Nachtegaal, A. H. Clark, O. Kröcher and D. Ferri, Preparation, quantification, and reaction of Pd hydrides on Pd/Al_2O_3 in liquid environment, *ACS Catal.*, 2023, **13**, 3323–3332.

29 M. Yarar, A. Bouziani and D. Uner, Pd as a reduction promoter for TiO_2: Oxygen and hydrogen transport at 2D and 3D Pd interfaces with TiO_2 monitored by TPR, operando 1H NMR and CO oxidation studies, *Catal. Commun.*, 2023, **174**, 106580.

30 R. W. Dorn, L. O. Mark, I. Hung, M. C. Cendejas, Y. Xu, P. L. Gor'kov, W. Mao, F. Ibrahim, Z. Gan, I. Hermans and A. J. Rossini, An atomistic picture of boron oxide catalysts for oxidative dehydrogenation revealed by ultrahigh field 11B-

17O solid-state NMR spectroscopy, *J. Am. Chem. Soc.*, 2022, **144**, 18766–18771.

31 R. W. Dorn, M. C. Cendejas, K. Chen, I. Hung, N. R. Altvater, W. P. McDermott, Z. Gan, I. Hermans and A. J. Rossini, Structure determination of boron-based oxidative dehydrogenation heterogeneous catalysts with ultra-high field 35.2 T 11B solid-state NMR spectroscopy, *ACS Catal.*, 2020, **10**, 13852–13866.

32 G. Bilgiç, N. Korkmaz, M. Şahin and A. Karadağ, Synthesis, structural, and electrochemical properties of boron-based ionic liquid, *Ionics*, 2022, **28**, 3289–3300.

33 S. Liu, Y. Deng, L. Fu, L. Huang, L. Ouyang and S. Yuan, Understanding the role of boron on the interface modulation of the Pd/TiO2 catalyst for direct synthesis of H2O2, *ACS Sustainable Chem. Eng.*, 2022, **10**, 3264–3275.

34 R. Liu, C. Wang, Y. Yan, R. Wang and G. Chen, Reversed charge transfer to modulate the d-band center of Pd for efficient direct H2O2 synthesis, *ACS Catal.*, 2024, **14**, 3955–3965.

35 R. Rajesh, S. Lingalwar, P. Challa, P. Balla, B. Shanmugavelu, V. P. Sruthi, S. Kim, S. Senthilkumar and V. Perupogu, Low-temperature total oxidation of propane using silver-decorated MnO2 nanorods, *ACS Appl. Nano Mater.*, 2023, **6**, 12258–12270.

36 M. Shamzhy, B. Gil, M. Opanasenko, W. J. Roth and J. Čejka, MWW and MFI frameworks as model layered zeolites: structures, transformations, properties, and activity, *ACS Catal.*, 2021, **11**, 2366–2396.

37 M. G. Bridelli and P. R. Crippa, Infrared and water sorption studies of the hydration structure and mechanism in natural and synthetic melanin, *J. Phys. Chem. B*, 2010, **114**, 9381–9390.

38 J. Wu, M. Lin, X. Cong, H. Liu and P. Tan, Raman spectroscopy of graphene-based materials and its applications in related devices, *Chem. Soc. Rev.*, 2018, **47**, 1822.

39 W. Cen, Y. Liu, Z. Wu, J. Liu, H. Wang and X. Weng, Cl Species Cl Species transformation on CeO_2(111) surface and its effects on CVOCs catalytic abatement: A first-principles investigation, *J. Phys. Chem. C*, 2014, **118**, 6758–6766.

40 L. M. Petrick, S. Sabach and Y. Dubowski, Degradation of VX surrogate profenofos on surfaces via in situ photo-oxidation, *Environ. Sci. Technol.*, 2013, **47**, 8751–8758.